Effect of hydrostatic pressure and alloying on thermoelectric properties of van der Waals solid KMgSb: An *ab initio* study

Vikrant Chaudhary [1], Tulika Maitra,[2] Tashi Nautiyal [2], Jeroen van den Brink,[3,4] and Hem C. Kandpal [1,*]

[1]*Department of Chemistry, Indian Institute of Technology Roorkee, Roorkee-247667, Uttarakhand, India*
[2]*Department of Physics, Indian Institute of Technology Roorkee, Roorkee-247667, Uttarakhand, India*
[3]*Institute for Theoretical Solid State Physics, IFW Dresden, Helmholtzstrasse 20, 01069 Dresden, Germany*
[4]*Institute for Theoretical Physics and Würzburg-Dresden Cluster of Excellence ct.qmat, Technische Universität Dresden, 01069 Dresden, Germany*

(Received 12 January 2023; accepted 28 August 2023; published 19 September 2023)

Using a combined approach of first-principles and Boltzmann transport theory, we conducted a systematic investigation of the thermal and electrical transport properties of the unexplored ternary quasi-two-dimensional KMgSb system of the KMgX (X = P, As, Sb, and Bi) family. In this paper, we present the transport properties of KMgSb under the influence of hydrostatic pressure and alloy engineering. At a carrier concentration of $\sim 8 \times 10^{19}$ cm^{-3}, we observed a close match in the figure of merit (zT; ~0.75, at 900 K) for both n-type and p-type KMgSb, making it an attractive choice for engineering thermoelectric devices with uniform materials in both legs. This characteristic is particularly advantageous for high-performance thermoelectric applications. Additionally, as pressure decreases, the zT value exhibits an increasing trend, further enhancing its potential for use in thermoelectric devices. Substitutional doping (replacing 50% of Sb atoms with Bi atoms) resulted in a significant ~49% (in-plane) increase in the peak thermoelectric figure of merit. Notably, after alloy engineering, the maximum figure-of-merit value obtained reached ~1.45 at 900 K temperature. Hydrostatic pressure emerges as an effective tool for tuning the lattice thermal conductivity κ_L. Our observations indicate that negative-pressure-like effects can be achieved through the chemical doping of larger atoms, especially when investigating κ_L properties. Through our computational investigation, we elucidate that hydrostatic pressure and alloy engineering hold the potential to dramatically enhance thermoelectric performance in this compound.

DOI: 10.1103/PhysRevMaterials.7.095401

I. INTRODUCTION

Thermometric materials have been around for many decades now. Many materials have been developed and identified for thermoelectric-device-based applications [1–9]. The performance and efficiency of thermoelectric materials are judged using a dimensionless figure of merit $zT = S^2\sigma T/(\kappa_e + \kappa_L)$, where S, σ, κ_e, and κ_L are the Seebeck coefficient, electrical conductivity, electronic thermal conductivity, and lattice thermal conductivity, respectively. Among the many promising materials [7,10–18], the materials that are layered in nature, such as SnSe, show a high zT value due to their low thermal conductivity [2]. Thus the quasi-two-dimensional (quasi-2D) nature of layered materials leads to improved thermoelectric performance, and such materials are widely used in thermoelectric devices. SnSe is an example of a layered material where high zT values have been reported in n-type as well as p-type doping regions. The layered SnSe has shown exemplary thermoelectric performance in both single crystals and polycrystalline phases [19]. With the same motive, we have studied the less explored KMgSb from the KMgX (X = P, As, Sb, and Bi) family, where the compounds have a quasi-2D type of crystal structure. As per our knowledge, all the members of the KMgX family, except KMgN, have been experimentally realized [20].

The topological [21] and thermoelectric [22] properties of KMgBi are well explored among all members in the family. KMgBi has been reported to host type-I Dirac points [21] and in another study was reported as a narrow-band-gap (~11.2 meV) semiconductor [23]. Contrary to this, a study based on density functional theory (DFT) has reported that KMgBi has a larger band gap (~280 meV) and shows a high zT value (~2.21) with p-type doping, which is expected to improve further with alloy engineering [22].

Besides KMgBi, a few studies have been reported related to other members of the KMgX (X = P, As, Sb, and Bi) family in hexagonal, orthorhombic, and half-Heusler phases. The thermoelectric properties of KMgP have been investigated in the half-Heusler thin film [24] and the MoS_2-type 2D structure [25]. The ferroelectric and antiferroelectric properties of KMgSb and KMgBi have been reported in the hexagonal [26] and orthorhombic [27] phases, respectively. In another study, the optical and elastic properties of KMgX (X = P, As, Sb, and Bi) have been explored in a hypothetical half-Heusler structure [28]. Apart from these, no thermal and electronic transport studies have been reported, as per our knowledge, in the abovementioned or experimentally realized tetragonal ($P4/nmm$) structures. Thus we have investigated the thermoelectric transport of KMgSb from the KMgX family in the less studied and experimentally realized quasi-2D tetragonal structure [20]. We find that as we go down in the KMgX family, the band gap value lowers, and this tunability can play an

*Corresponding author: hem.kandpal@cy.iitr.ac.in

important role in getting a good thermoelectric performance. The known studies on KMgBi [21,22] further motivated us to investigate KMgSb in the quasi-2D structure.

Over time, many techniques have been used to enhance the thermoelectric performance of materials. For example, PbTe and PbTe-based materials have been developed as high-performance thermoelectric materials by optimizing phonon and charge transport. These techniques include tuning the Fermi level by changing the carrier density, increasing the effective mass by band structure engineering, decreasing the lattice thermal conductivity by nanostructuring, etc. [29]. Another promising way of improving thermoelectric performance is alloy engineering [30].

We picked KMgSb as a candidate material for this study. In this paper, we have investigated the effect of hydrostatic pressure and isoelectronic doping (at the Sb sites) on the thermoelectric performance of KMgSb. The hydrostatic pressure results in varying interlayer spacing in the quasi-2D KMgSb, which affects the zT value significantly. As, Bi, and Sb are isoelectronic elements, and doping Sb and Bi helps only in tuning the volume and in generating substitutional defects. Moreover, the increased volume caused by chemical doping can be thought of as a condition created by negative pressure, which is also an important parameter and helps in the enhancement of thermoelectric performance. Further details are given in Sec. III.

II. COMPUTATIONAL DETAILS

The computations performed in this paper have three major components, namely, (a) DFT for electronic band structure and density functional perturbation theory (DFPT) for mechanical and dielectric properties, (b) phonon or lattice dynamics, and (c) the scattering rates and transport properties.

The DFT and DFPT calculations were performed using the Vienna *ab initio* simulation package (VASP) [31–34]. The all-electron projector augmented wave method [35,36] was adopted with a plane-wave cutoff energy of 550 eV, and a breaking condition of 10^{-8} eV on the self-consistent field (SCF) cycles was used. We have used the generalized gradient approximation (GGA) of Perdew, Burke, and Ernzerhof (PBE) [37], the revised PBE for solids (PBEsol) [38], and the Heyd-Scuseria-Ernzerhof 2006 (HSE06) [39] hybrid functional for the exchange-correlation part. Since KMgX family compounds are layered in nature, the van der Waals density functional (optB86b-vdW) [40] is used on top of the PBE and HSE06 functionals. All crystal structures are optimized on a $21 \times 21 \times 15$ k mesh. During the ionic relaxation, the forces were relaxed with a breaking condition of 0.01 eV/Å. Furthermore, the mechanical and dielectric properties were calculated using the DFPT module of VASP, and the results were used for scattering rate evaluation.

The phonon band structures and Grüneisen parameters were obtained using the harmonic approximation in the PHONOPY package [41] and the DFPT module of VASP. For Grüneisen parameter calculations, the volume of the unit cell was changed by approximately $\pm 1.0\%$. We obtained the lattice thermal conductivity κ_L using the PHONO3PY [42] and SHENGBTE [43,44] packages on top of the DFT results from VASP. A $2 \times 2 \times 2$ supercell was used to calculate the third-order [44] and fourth-order [45–47] anharmonic interatomic force constants (IFCs). The second-order IFCs were obtained using PHONOPY by generating large supercell ($3 \times 3 \times 2$) structures. PHONO3PY gives results within the relaxation time approximation (RTA), whereas SHENGBTE allows us to calculate κ_L using the RTA as well as the iterative method. We observed a close agreement between the κ_L values obtained from the two methods. The compounds studied in this paper are ionic in nature. Thus we included nonanalytical corrections in our calculations.

The last component in computations is related to the scattering rates and transport properties, which are calculated using the AMSET code [48]. AMSET takes mechanical, piezoelectric, and dielectric properties, wave functions, band structure, and deformation potential as input, which we obtained from the VASP calculations. The electronic and thermal transport properties are obtained by numerically solving the linearized Boltzmann transport equations (BTEs). For a very long time, these BTEs were solved within the constant-relaxation-time approach (CRTA) due to the complex nature of the scattering processes. In AMSET, the scattering rates are obtained using Fermi's golden rule,

$$\tau_{i\to f}^{-1} = \frac{2\pi}{\hbar}|g_{fi}(\mathbf{k},\mathbf{q})|^2\delta(\epsilon_i - \epsilon_f), \tag{1}$$

where i (f) is the initial (final) state, τ is the relaxation time, g is the coupling matrix, and ϵ_i (ϵ_f) is the initial (final) energy of the electron. The g matrices are the scattering rate calculations' most significant and complex part. These matrices were obtained using acoustic deformation potential (ADP), ionized impurity (IMP), and polar optical phonon (POP) scattering mechanisms in this paper. The ADP and IMP are elastic processes, while POP is inelastic [48]. The relaxation time obtained is automatically used in various transport properties, which are obtained by solving the Boltzmann transport equations module of AMSET. Various transport coefficients are obtained from the generalized transport equation

$$\mathcal{L}^{\alpha}(\mu,T) = q^2\int \Sigma(\epsilon)\,(\epsilon-\mu)^{\alpha}\left(-\frac{\partial f^0(\epsilon,T)}{\partial\epsilon}\right)d\epsilon, \tag{2}$$

where q, $\Sigma(\epsilon)$, μ, and $f^0(\epsilon,T)$ are the electronic charge, spectral conductivity, chemical potential, and Fermi-Dirac distribution function, respectively [48–50]. The Seebeck coefficient S, the electronic conductivity σ, and the electronic component of the thermal conductivity κ_e are given by $\frac{1}{qT}\frac{\mathcal{L}^1}{\mathcal{L}^0}$, $\mathcal{L}^0$, and $\frac{1}{q^2T}[\frac{(\mathcal{L}^1)^2}{\mathcal{L}^0} - \mathcal{L}^2]$, respectively.

III. RESULTS AND DISCUSSION

A. Structural analysis

The compounds of the KMgX family (X = P, As, Sb, and Bi) crystallize in the $P4/nmm$ space group (No. 129) [20]. K, Mg, and X occupy the $2c$ (0, 0.5, ~0.65), $2a$ (0, 0, 0), and $2c$ (0, 0.5, ~0.20) sites, respectively. The z components of the sites occupied by K and X are free positions, which we have relaxed during the structural optimization. The structures of KMgX are layered in the c direction, consisting of alternating K and Mg-X layers. In the Mg-X layer, Mg and X atoms form edge-sharing tetrahedra, as shown in Fig. 1. Since K

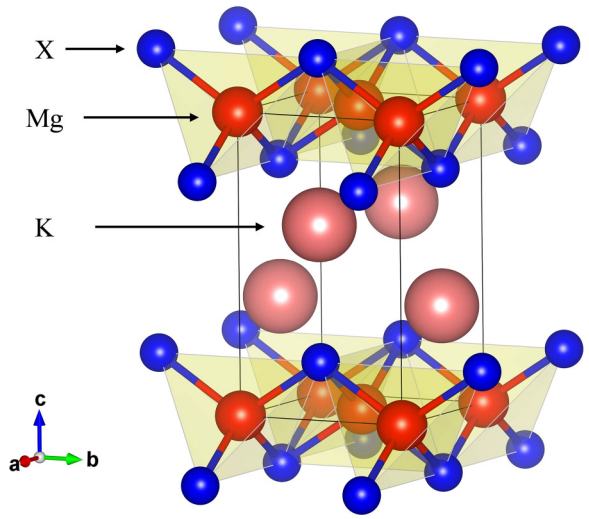

FIG. 1. The crystal structure of KMgX (X = P, As, Sb, and Bi) in the $P4/nmm$ space group.

is an alkali metal, it tends to give an electron to the MgX tetrahedron, resulting in an electrostatic interaction between K^+ and $[MgX]^-$. This electrostatic interaction is weaker than the covalent bond between Mg and X atoms due to the large separation between K and Mg-X layers.

The interaction between the layers of KMgX is a van der Waals interaction in nature. Therefore it becomes inevitable to exclude van der Waals corrections in DFT calculations. The unit cell parameters were fully relaxed using PBE, PBEsol, PBE with optB86b-vdW, HSE06, and HSE06 with optB86b-vdW exchange-correlation functionals, as given in Table I. The lattice parameters obtained with the optB86b-vdW correction and using the HSE06 and PBE functionals are in excellent agreement with the experimental values. As we go down the table, PBE with optB8b-vdW gives a more accurate value, and the most accurate results are obtained for KMgBi.

TABLE II. The band gaps of the KMgX (X = P, As, Sb, and Bi) family compounds and related alloys. The band gaps in parentheses are obtained by including spin-orbit coupling (SOC) in the calculations. The experimental band gap of KMgBi is ∼0.011 eV [23].

	Band gap E_g (eV)			
Composition[a]	PBE	PBE[b]	HSE06	HSE06[b]
KMgP	1.70 (1.63)	1.80 (2.02)	2.49 (2.47)	2.55 (2.78)
KMgAs	1.12 (1.04)	1.25 (1.39)	1.92 (1.83)	1.96 (2.11)
KMgSb	1.26 (1.07)	1.34 (1.25)	1.93 (1.74)	1.96 (1.87)
$KMgSb_{0.5}Bi_{0.5}$	0.76 (0.38)	0.89 (0.69)	1.43 (1.00)	1.50 (1.27)
KMgBi	0.31 (0.00)	0.49 (0.16)	0.93 (0.35)	1.03 (0.64)

[a]KMgN is not experimentally known and hence is not included in this paper.
[b]With the optB86b-vdW correction.

The PBE (with optB86b-vdW) calculated a lattice constant of KMgBi differs only by 0.001 Å from the experimental value, and c matches exactly up to three decimal points as given in Table I. Without the van der Waals corrections, the c lattice parameter differs significantly from the experimental value.

The band gap is another parameter that we have tested with different exchange-correlation functionals. We only have the experimental band gap (∼11.2 meV) for KMgBi, obtained from resistivity data measured between 40 and 100 K [23]. The band gap value obtained from PBE with optB86b-vdW seems to be the best prediction for KMgBi, considering many approximations that DFT is based on. The band gap values of various compositions are given in Table II.

We thoroughly scanned the KMgX family compounds and found that KMgSb is a good candidate for pressure study and alloy engineering. KMgBi is reported to show good thermoelectric performance [22]. However, the results published on KMgBi are based on PBE optimized crystal structure, which lacks the inclusion of van der Waal's correction mandatory for this family of compounds. The PBE optimized lattice

TABLE I. The lattice parameters of the KMgX (X = P, As, Sb, and Bi) family members and related alloys. The values in parentheses are relative percentage errors with respect to the experimental lattice constants. NA, not available.

		Lattice parameter value (Å)					
Composition[a]	Lattice parameter	PBE	PBEsol	PBE[b]	HSE06	HSE06[b]	Expt. [20]
KMgP	a	4.462 (0.36)	4.426 (−0.45)	4.426 (−0.45)	4.436 (−0.22)	4.428 (−0.40)	4.446
	c	7.599 (0.73)	7.526 (−0.24)	7.532 (−0.16)	7.605 (0.81)	7.536 (−0.11)	7.544
KMgAs	a	4.577 (0.68)	4.526 (−0.44)	4.530 (−0.35)	4.546 (0.00)	4.536 (−0.22)	4.546
	c	7.872 (2.02)	7.736 (0.26)	7.742 (0.34)	7.796 (1.04)	7.738 (0.28)	7.716
KMgSb	a	4.840 (0.58)	4.781 (−0.64)	4.794 (−0.37)	4.803 (−0.19)	4.794 (−0.37)	4.812
	c	8.341 (1.69)	8.223 (0.26)	8.221 (0.23)	8.258 (0.68)	8.204 (0.02)	8.202
$KMgSb_{0.5}Bi_{0.5}$	a	4.888	4.820	4.834	4.848	4.839	NA
	c	8.446	8.311	8.306	8.355	8.288	NA
KMgBi	a	4.933 (1.06)	4.870 (−0.22)	4.882 (0.02)	4.896 (0.31)	4.885 (0.08)	4.881
	c	8.545 (1.94)	8.397 (0.18)	8.382 (0.00)	8.452 (0.84)	8.365 (−0.20)	8.382

[a]KMgN is not experimentally known and hence is not included in this paper.
[b]With the optB86b-vdW correction.

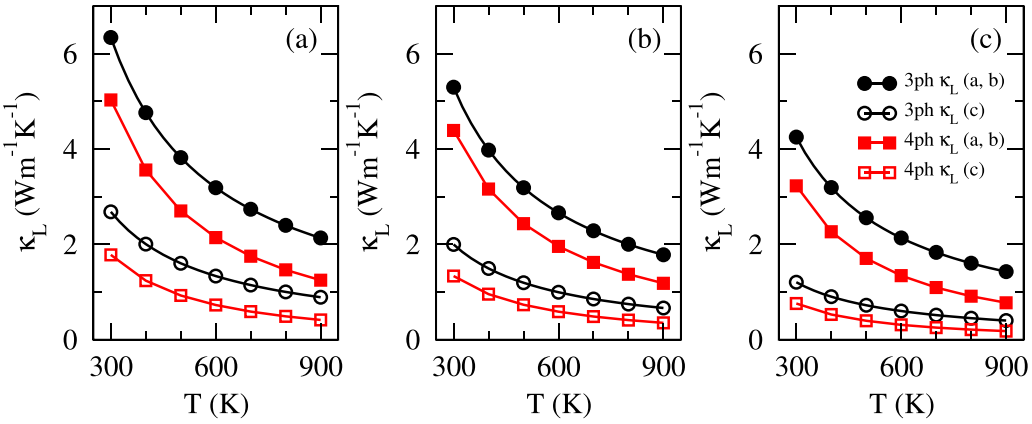

FIG. 2. The lattice thermal conductivity κ_L of KMgSb at (a) 1.0 GPa, (b) ambient, and (c) −1.0 GPa pressure. The black curves show the κ_L calculated using third-order IFCs, and red curves represent values obtained using fourth- and third-order IFCs. Here, 3ph, three-phonon scattering; 4ph, four-phonon scattering; *a*, *b*, and *c* are the lattice parameters.

constants of KMgBi show a large deviation from experimental values, as shown in Table I. Also, the transport properties of KMgBi reported in earlier work were obtained by scaling the PBE band gap to the HSE06 + Hedin's *GW* approximation + spin-orbit coupling (HSE06+GW + SOC) band gap, keeping the band curvature fixed. This approach should not reflect the effect of HSE06 and GW in the final transport results. Also, the band gap of KMgBi obtained using HSE06+GW + SOC is overestimated (∼280 meV) [22]. The band gap of KMgBi that we obtain in this paper with GGA+optB86b-vdW+SOC is quantitatively the best theoretically predicted value. Also, the predicted lattice constants with PBE+optB86b-vdW are the most accurate (closest to experimental) values. Our approach is to work with the functional that gives the most accurate lattice constants and band gap values. In light of the available studies, we have picked the unexplored KMgSb from the family and carried out a detailed investigation to understand the thermoelectric transport in the KMg*X* family. In this paper, we selected PBE with optB86b-vdW corrections for all the calculations, including phonon and charge transport evaluation. Using alloy engineering (Bi doping in KMgSb in this paper), a composition with promising thermoelectric transport properties is reported. The pressure study and alloy engineering (Bi doping in KMgSb) are discussed in the following sections of this paper.

B. KMgSb under hydrostatic pressure

The KMgSb has a low bulk modulus (∼25 GPa), as we found in our calculations. The low bulk modulus indicates that KMgSb is a low-strength material and large values of hydrostatic pressure will possibly change the crystal structure of the compound. Herein, we are not interested in a pressure-driven phase transition. Therefore we have limited our study to −1.0 and 1.0 GPa pressure. To understand the effect of the pressure on the unit cell, the change in lattice parameters of KMgSb and KMgBi with pressure is given in the Supplemental Material (SM) [51].

The phonon band structure and mode Grüneisen parameter γ are the key tools to understand the various aspects of lattice dynamics, which we calculated using the PHONOPY package [41]. The mode Grüneisen parameter is a direct measure of the degree of anharmonicity in phonon modes. A larger value of γ leads to a low κ_L, as per the inverse square relation ($\kappa_L \propto 1/\gamma^2$) [52]. The maximum value of γ (∼1.75 at ambient pressure) in the acoustic region (below ∼2.4 THz) rises to ∼2.25 at −1.0 GPa (see SM). We are focusing on the acoustic region as it is clear that these modes have their maximum contribution in the κ_L of KMgSb (see SM). This rise in the γ value indicates increasing anharmonicity in the vibration modes and leads to a significant drop in the κ_L of KMgSb (Fig. 2). Thus there is an average and directional κ_L decrease under the application of negative pressure. This reduction is purely due to the change in the bonding strength when the volume of the cell increases. The ambient-pressure κ_L obtained in our calculations is higher than the recently reported values [53]. The discrepancy is possibly due to the different techniques used for κ_L calculations. Moreover, the methods used by She *et al.* [53] are also known to underestimate κ_L in some cases [54,55]. The reduced κ_L helps improve the thermoelectric figure of merit (zT), subject to the condition that the power factor (PF = $S^2\sigma$) remains unchanged or increases.

We observed two increasing trends in the thermoelectric-figure-of-merit (zT) values of KMgSb, one with increasing pressure (in the *c* direction and at ∼6×10^{20} cm^{-3} *n*-type doping) and the other with decreasing pressure (at ∼3.9×10^{19} cm^{-3} in the *n*-type regions and at ∼2.5×10^{20} cm^{-3} in the *p*-type regions). Now, we will explain these two trends one by one. The peak value of the PF of KMgSb is found to increase with pressure in all directions and in both doping regions. In contrast, little change is observed in the electronic and lattice thermal conductivity. Therefore, at 900 K, the enhancement in the zT value (see Fig. 4, discussed later) in the *n*-type doping is solely due to the increased PF. The electrical conductivity σ shows negligible variation with pressure; hence the changes in the PF are primarily due to the Seebeck coefficient *S*, as shown in the SM. The pressure changes the band dispersion in the $\Gamma \rightarrow Z$ direction of the conduction region, which is shown in Fig. 3. The bands inside the red circle (Fig. 3) are flatter at 1.0 GPa pressure than they are at ambient and −1.0 GPa pressure, which results in the increasing effective mass of electrons and Seebeck coefficient of KMgSb. This

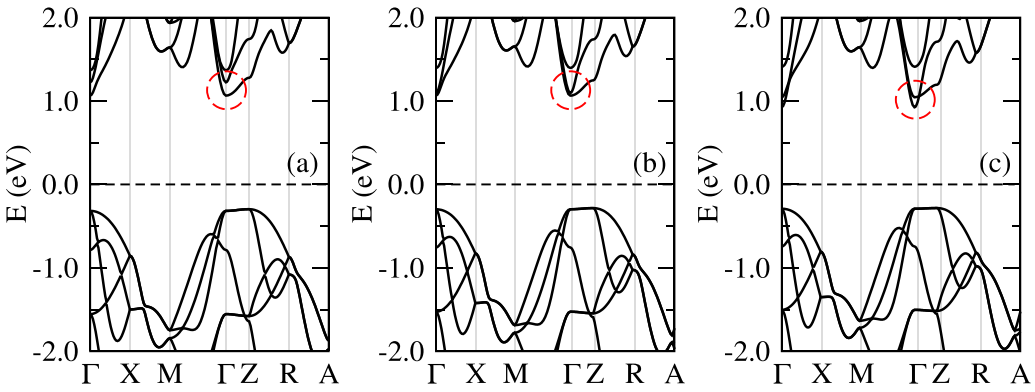

FIG. 3. The electronic band structures of KMgSb with van der Waals corrections and at (a) 1.0 GPa, (b) ambient, and (c) −1.0 GPa pressure. These band structures are obtained without including spin-orbit coupling (SOC) in the calculations.

leads to a sharp increase in the PF along the c direction and in the n-type doping region, increasing the zT value.

In the second case, the peak zT values are found to increase with decreasing pressure in both doping regions (see Fig. 4). This increase in zT value is primarily due to the decreasing κ_L (Fig. 2) because the PF does not increase as we go towards negative pressure. Therefore the zT value can be increased by applying hydrostatic pressure. In experiments, positive pressure can be generated using a diamond anvil cell, whereas negative pressure generation seems extremely challenging. The negative pressure results in increased unit cell volume, which can be achieved by chemically doping larger atoms in place of smaller ones. Herein, we selected the Bi atom to replace Sb in KMgSb. Since Bi and Sb are isoelectronic, we expect that the alloying will only change the unit cell size and not the carrier concentration. This substitution is one way to create a negative-pressure-like effect in experimental synthesis. As an interesting observation, we found that the κ_L at −1.0 GPa matches closely (in the a-b plane) with the κ_L of $KMgSb_{0.5}Bi_{0.5}$.

The n-type and p-type zT values of KMgSb at $\sim 8 \times 10^{19}$ cm^{-3} doping level are in close agreement. The ambient-pressure zT value in the n-type [Fig. 4(c)] and p-type [Fig. 4(d)] regions is ∼0.75 at $\sim 8 \times 10^{19}$ cm^{-3}. This is an exciting feature of KMgSb, which is highly desirable in real-life thermoelectric device-based applications. Hence KMgSb may be used as a p-type leg as well as an n-type leg of a thermoelectric device. Moreover, KMgSb is a p-type thermoelectric material above 10^{20} cm^{-3} carrier concentration. Most of the high-performance thermoelectric materials being reported are of n type, which makes KMgSb interesting as it may be used as a p-type leg in thermoelectric devices.

C. Effect of alloying

Considering that the κ_L of KMgSb decreases as we go towards negative pressure, it is worth exploring further. In a recent computational study, KMgBi was reported as an excellent thermoelectric material with a desirably high zT value (>2.0) [23]. KMgSb being closer to KMgBi in size (than, e.g., KMgAs) makes KMgSb an exciting candidate for experimentalists to replace Sb with Bi and fine-tune the thermal and electronic properties. We designed a composition by replacing 50% of the Sb atoms with Bi atoms. At −1.0 GPa, the a and c lattice constants of KMgSb are 4.853 and 8.388 Å, respectively. The lattice constants of $KMgSb_{0.5}Bi_{0.5}$ (see Table I) match closely with the lattice constants of KMgSb at −1.0 GPa. The difference between the a values of $KMgSb_{0.5}Bi_{0.5}$ and KMgSb (at −1.0 GPa) is 0.019 Å, and the difference between their c values is 0.082 Å. Therefore, by doping 50% Bi in KMgSb, we have designed a composition of a size similar to that of KMgSb at −1.0 GPa.

The phonon band structure of $KMgSb_{0.5}Bi_{0.5}$ contains 18 bands, where the three lowest frequency bands [orange bands in Fig. 5(a)] originating from the Γ point are the acoustic bands. All three acoustic modes—two transverse acoustic (TA) and one longitudinal acoustic (LA)—are seen up to a frequency of ∼2 THz. These acoustic modes carry most of the heat in the crystal as observed in the cumulative lattice thermal conductivity κ_c shown in Fig. 5(d). The phonon density of states (PhDOS) confirms that the acoustic modes are dominated by Sb atoms in KMgSb (see SM). The acoustic and optical branches of the phonon bands of KMgSb become degenerate above 2.0 THz frequency. The doping of Bi in KMgSb is directly reflected in the acoustic branches of phonon bands. Bi doping lowers the maximum frequency of the acoustic modes from ∼2.4 to ∼2.0 THz and separates the acoustic band from the optical bands. After Bi doping, the mode Grüneisen parameter [Fig. 5(b)] shows increased anharmonicity in the low-frequency modes very similar to that of KMgSb at −1.0 GPa, and these modes contribute more than 75% (a-b plane) and 85% (c direction) in cumulative lattice thermal conductivity (κ_c) as shown in Fig. 5(d). Bi doping does two interesting things: (a) increase the size of the cell and (b) cause strain in the lattice. Therefore replacing Sb with Bi compensates for the negative pressure and also increases the anharmonicity in phonon modes due to the strain in the lattice from the substitutional defects. These factors lead to a decrease in the κ_L after doping Bi in KMgSb as shown in Fig. 5(c).

In Fig. 6, the band structure of $KMgSb_{0.5}Bi_{0.5}$ is shown, where flat (in the $\Gamma \rightarrow Z$ direction and valence region) as well as largely dispersive (in the conduction region) bands are seen. The band gap of $KMgSb_{0.5}Bi_{0.5}$ is ∼0.89 eV without spin-orbit coupling (SOC), which drops to ∼0.69 eV with SOC. Bi doping has significantly reduced the band gap. Such

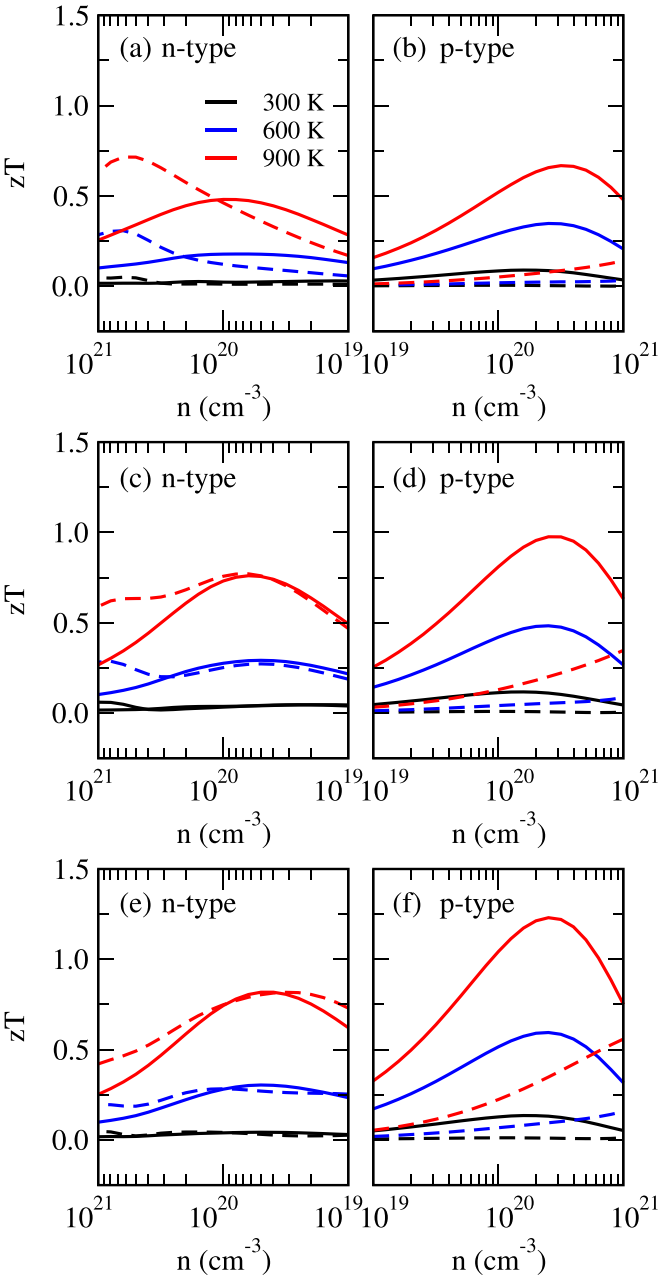

FIG. 4. The thermoelectric figure of merit (without SOC) of KMgSb at (a) and (b) 1.0 GPa, (c) and (d) ambient, and (e) and (f) −1.0 GPa pressure. The black, blue, and red curves represent zT at 300, 600, and 900 K temperatures, respectively. The solid and dashed curves show zT in the *a*-*b* plane and along the *c* direction, respectively. On the *x* axis, we have used *n* for the doping level.

tunability of the band gap (with doping) is highly desirable when designing materials for thermoelectric applications. In Fig. 7, present the power factor (PF), total thermal conductivity ($\kappa_e + \kappa_L$), and zT of $KMgSb_{0.5}Bi_{0.5}$. The zT value of KMgSb and $KMgSb_{0.5}Bi_{0.5}$ increases with temperature. At 900 K, the peak zT value of $KMgSb_{0.5}Bi_{0.5}$ is ∼1.45, which is obtained in the *p*-type region as shown in Fig. 7(f). The κ_e values of KMgSb and $KMgSb_{0.5}Bi_{0.5}$ at 900 K closely match (see SM) at the doping level of the peak zT value, whereas a significant increase in PF ($S^2\sigma$) is observed after

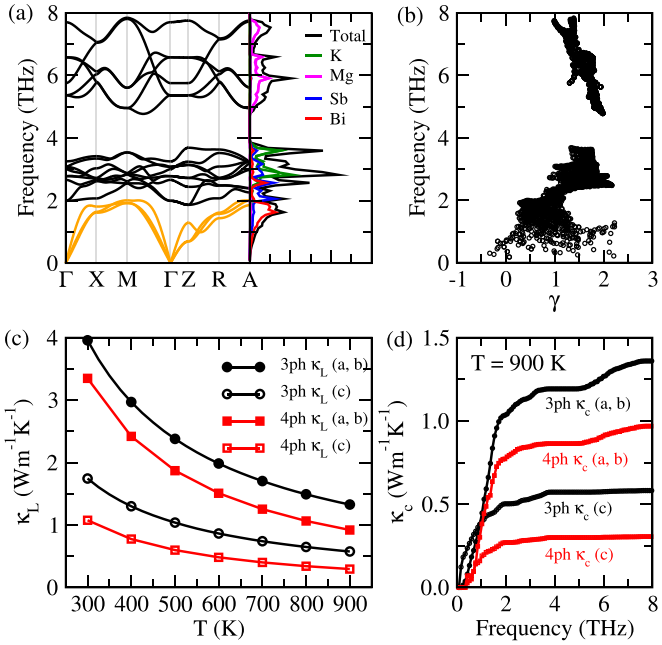

FIG. 5. (a) Phonon band structure and density of states (PhDOS), (b) Grüneisen parameter γ, (c) lattice thermal conductivity κ_L, and (d) cumulative lattice thermal conductivity κ_c of $KMgSb_{0.5}Bi_{0.5}$ at 900 K.

Bi doping. If we compare the peak zT values of KMgSb and $KMgSb_{0.5}Bi_{0.5}$ in the *p*-type region, an increase of ∼49% is obtained after alloy engineering. This increase in the zT value is due to the increased PF and reduced κ_L after Bi doping in KMgSb. As discussed above, KMgSb remains a *p*-type thermoelectric material under hydrostatic pressure. Bi doping enhances the zT value, and $KMgSb_{0.5}Bi_{0.5}$ becomes a potential high-performance *p*-type thermoelectric material, which is highly desirable for device engineering.

As discussed above, substitutional doping creates defects that increase phonon scattering and reduces κ_L, which is desirable for thermoelectric applications. We also investigated the thermoelectric transport of As-doped KMgSb but observed no significant increase or decrease in the peak zT value, even though the κ_L improves after As doping. The zT value

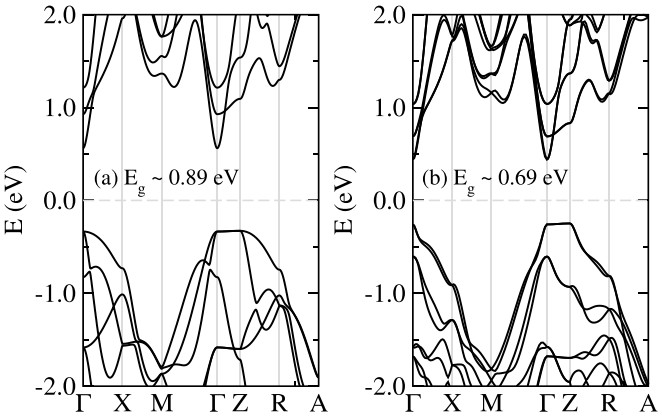

FIG. 6. The electronic band structure of $KMgSb_{0.5}Bi_{0.5}$ without (a) and with (b) spin-orbit coupling (SOC).

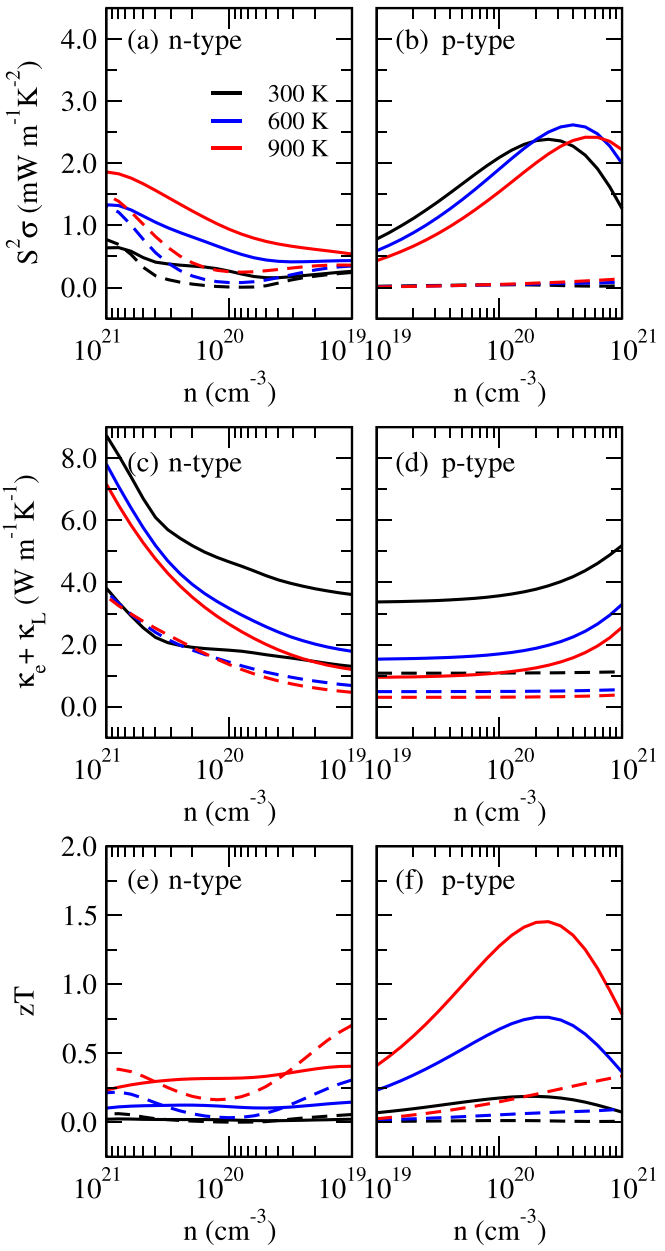

FIG. 7. (a) and (b) The power factor (PF), (c) and (d) thermal conductivity ($\kappa_e + \kappa_L$), and (e) and (f) thermoelectric figure of merit (zT) of $KMgSb_{0.5}Bi_{0.5}$. The black, blue, and red curves represent zT at 300, 600, and 900 K temperatures, respectively. The solid and dashed curves show zT in the *a*-*b* plane and along the *c* direction, respectively. On the *x* axis, we have used *n* for the doping level. These results are obtained without SOC.

of $KMgSb_{0.5}As_{0.5}$ remains close to the zT value of KMgSb at ambient pressure. The electronic and ionic properties of $KMgSb_{0.5}As_{0.5}$ are given in the SM.

One important aspect of thermoelectric transport is the electronic relaxation time, which is a complex phenomenon. As discussed in Sec. II, the CRTA was considered to be the most convenient and helpful choice in electronic transport calculations, but it comes with a cost as under CRTA, the Seebeck and Hall coefficients become independent of scattering rates [56]. Moreover, a constant value of τ cannot account for all the scattering processes involved in electronic transport. To gain insight, we have shown the scattering-mechanism-dependent relaxation time τ in Fig. 8. The overall electronic relaxation time is found to lie between $\sim 10^{-13}$ and $\sim 10^{-16}$ s, which arises primarily from the POP with a small contribution from ADP and IMP scattering mechanisms.

The results discussed above explain the impact of pressure and alloy engineering on thermal and electronic transport. The thermoelectric performance shows a huge improvement after Bi doping. The spin-orbit coupling (SOC) is also an important factor in transport properties. It requires a lot of resources to include SOC in all DFT, hybrid DFT, and thermal and electronic transport calculations. The Seebeck coefficient S, the electronic conductivity σ, and the electronic component of the thermal conductivity κ_e of KMgSb and $KMgSb_{0.5}Bi_{0.5}$ with and without SOC are given in the SM. The calculation of κ_L (including fourth-order IFCs) with SOC is extremely challenging and is not included in this paper. We observed that the SOC has a small effect on S, σ, and κ_e.

IV. SUMMARY AND CONCLUSIONS

In this paper, we started with the investigation of the crystal and electronic structure of the KMgX family (X = P, As, and Sb). All compounds of the KMgX family have van der Waals interaction along the *c* direction. The van der Waals interaction is treated with optB86b-vdW with the PBE functional, which we found to give lattice constants closely matching with the experimental values. The effect of hydrostatic pressure and alloy engineering on the electronic and thermal transport properties of KMgSb is investigated in this paper.

It is encouraging to note that the κ_L of KMgSb decreases under negative pressure, implying that the application of negative pressure would be helpful in improving the thermoelectric performance. We observed that the zT value shows two increasing trends with the applied pressure. The positive pressure improves the zT value in the *n*-type region and along the *c* direction. A significant increase in the zT values in the *n*-type region, as well as the *p*-type region, is observed with the negative pressure. Interestingly, the *n*-type and *p*-type zT values of KMgSb at ambient and -1.0 GPa pressure are in close agreement at $\sim 8 \times 10^{19}$ cm^{-3} carrier concentration. This is an important feature that is desirable and can be utilized in thermoelectric device engineering.

Pressure plays an important role. Negative pressure, which is very challenging experimentally, increases the volume of the cell. In order to bring in the negative-pressure-like effect, we substituted 50% Sb with Bi atoms. The alloy engineering does improve thermoelectric performance dramatically. Bi doping decreases the κ_L but increases the power factor, and the overall effect leads to an ~49% increase in the zT value in the *a*-*b* plane and *p*-type doping region. The κ_L (in the *a*-*b* plane) of $KMgSb_{0.5}Bi_{0.5}$ matches well with the κ_L of KMgSb at -1.0 GPa pressure. Therefore the negative-pressure-like effect can possibly be obtained via chemical doping, at least as far as phonon transport is concerned. To conclude, hydrostatic pressure and alloy engineering help in improving the thermoelectric performance of the quasi-2D material KMgSb. Also, KMgSb can be used as an *n*-type as well as *p*-type thermoelectric material.

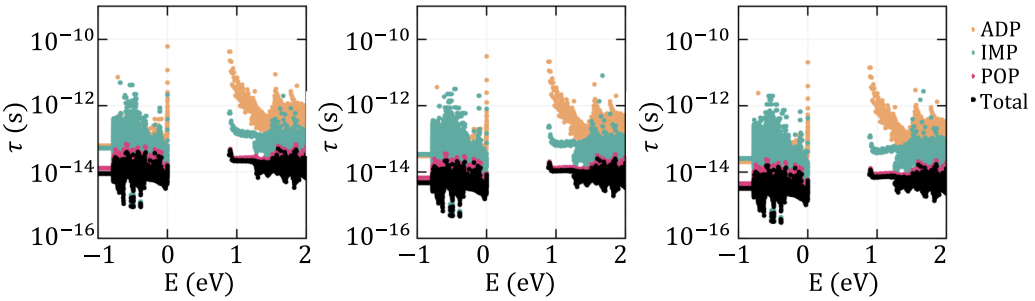

FIG. 8. The scattering-mechanism-dependent electronic relaxation time τ in $KMgSb_{0.5}Bi_{0.5}$, calculated at 300, 600, and 900 K for a 1.26×10^{20} cm^{-3} p-type carrier concentration.

ACKNOWLEDGMENTS

This work used the Supercomputing facility of IIT Roorkee established under the National Supercomputing Mission (NSM), Government of India, and supported by the Centre for Development of Advanced Computing (CDAC), Pune, India. We have also used other computational facilities provided by the Institute Computer Center (ICC), IIT Roorkee. V.C. wishes to acknowledge financial support received from the Ministry of Education, Government of India.

[1] G. J. Snyder and E. S. Toberer, Complex thermoelectric materials, Nat. Mater. **7**, 105 (2008).

[2] J. Wei, L. Yang, Z. Ma, P. Song, M. Zhang, J. Ma, F. Yang, and X. Wang, Review of current high-ZT thermoelectric materials, J. Mater. Sci. **55**, 12642 (2020).

[3] S. I. Kim, K. H. Lee, H. A. Mun, H. S. Kim, S. W. Hwang, J. W. Roh, D. J. Yang, W. H. Shin, X. S. Li, Y. H. Lee, G. J. Snyder, and S. W. Kim, Dense dislocation arrays embedded in grain boundaries for high-performance bulk thermoelectrics, Science **348**, 109 (2015).

[4] B. Poudel, Q. Hao, Y. Ma, Y. Lan, A. Minnich, B. Yu, X. Yan, D. Wang, A. Muto, D. Vashaee, X. Chen, J. Liu, M. S. Dresselhaus, G. Chen, and Z. Ren, High-thermoelectric performance of nanostructured bismuth antimony telluride bulk alloys, Science **320**, 634 (2008).

[5] L. Hu, H. Wu, T. Zhu, C. Fu, J. He, P. Ying, and X. Zhao, Tuning multiscale microstructures to enhance thermoelectric performance of n-type bismuth-telluride-based solid solutions, Adv. Energy Mater. **5**, 1500411 (2015).

[6] H. Zhao, J. Sui, Z. Tang, Y. Lan, Q. Jie, D. Kraemer, K. McEnaney, A. Guloy, G. Chen, and Z. Ren, High thermoelectric performance of MgAgSb-based materials, Nano Energy **7**, 97 (2014).

[7] L.-D. Zhao, J. He, C.-I. Wu, T. P. Hogan, X. Zhou, C. Uher, V. P. Dravid, and M. G. Kanatzidis, Thermoelectrics with earth abundant elements: High performance p-type PbS nanostructured with SrS and CaS, J. Am. Chem. Soc. **134**, 7902 (2012).

[8] L.-D. Zhao, G. Tan, S. Hao, J. He, Y. Pei, H. Chi, H. Wang, S. Gong, H. Xu, V. P. Dravid, C. Uher, G. J. Snyder, C. Wolverton, and M. G. Kanatzidis, Ultrahigh power factor and thermoelectric performance in hole-doped single-crystal SnSe, Science **351**, 141 (2016).

[9] Y. Zhou and L.-D. Zhao, Promising thermoelectric bulk materials with 2D structures, Adv. Mater. **29**, 1702676 (2017).

[10] Z.-G. Chen, X. Shi, L.-D. Zhao, and J. Zou, High-performance SnSe thermoelectric materials: Progress and future challenge, Prog. Mater. Sci. **97**, 283 (2018).

[11] L.-D. Zhao, C. Chang, G. Tan, and M. G. Kanatzidis, SnSe: a remarkable new thermoelectric material, Energy Environ. Sci. **9**, 3044 (2016).

[12] L.-D. Zhao, X. Zhang, H. Wu, G. Tan, Y. Pei, Y. Xiao, C. Chang, D. Wu, H. Chi, L. Zheng, S. Gong, C. Uher, J. He, and M. G. Kanatzidis, Enhanced thermoelectric properties in the counter-doped SnTe system with strained endotaxial SrTe, J. Am. Chem. Soc. **138**, 2366 (2016).

[13] D. Wu, L.-D. Zhao, S. Hao, Q. Jiang, F. Zheng, J. W. Doak, H. Wu, H. Chi, Y. Gelbstein, C. Uher, C. Wolverton, M. Kanatzidis, and J. He, Origin of the high performance in GeTe-based thermoelectric materials upon Bi_2Te_3 doping, J. Am. Chem. Soc. **136**, 11412 (2014).

[14] B. Yu, M. Zebarjadi, H. Wang, K. Lukas, H. Wang, D. Wang, C. Opeil, M. Dresselhaus, G. Chen, and Z. Ren, Enhancement of thermoelectric properties by modulation-doping in silicon germanium alloy nanocomposites, Nano Lett. **12**, 2077 (2012).

[15] J. Xin, Y. Tang, Y. Liu, X. Zhao, H. Pan, and T. Zhu, Valleytronics in thermoelectric materials, npj Quantum Mater. **3**, 9 (2018).

[16] C. Fu, S. Bai, Y. Liu, Y. Tang, L. Chen, X. Zhao, and T. Zhu, Realizing high figure of merit in heavy-band p-type half-Heusler thermoelectric materials, Nat. Commun. **6**, 8144 (2015).

[17] X. Yan, W. Liu, S. Chen, H. Wang, Q. Zhang, G. Chen, and Z. Ren, Thermoelectric property study of nanostructured p-type half-Heuslers (Hf, Zr, Ti)$CoSb_{0.8}Sn_{0.2}$, Adv. Energy Mater. **3**, 1195 (2013).

[18] M. K. Brod, S. Guo, Y. Zhang, and G. J. Snyder, Explaining the electronic band structure of half-Heusler thermoelectric semiconductors for engineering high valley degeneracy, MRS Bull. **47**, 573 (2022).

[19] S. Chandra, U. Bhat, P. Dutta, A. Bhardwaj, R. Datta, and K. Biswas, Modular nanostructures facilitate low thermal conductivity and ultra-high thermoelectric performance in n-type SnSe, Adv. Mater. **34**, 2203725 (2022).

[20] R. Vogel and H.-U. Schuster, Neue elektrovalente ternäre Verbindungen des Kaliums mit Magnesium und Elementen der 5. Hauptgruppe / New ternary compounds of potassium with magnesium and elements of the 5. main group, Z. Naturforsch. B: Anorg. Chem. Org. Chem. **34**, 1719 (1979).

[21] C. Le, S. Qin, X. Wu, X. Dai, P. Fu, C. Fang, and J. Hu, Three-dimensional topological critical dirac semimetal in AMgBi (A = K, Rb, Cs), Phys. Rev. B **96**, 115121 (2017).

[22] Vikram, B. Sahni, A. Jain, and A. Alam, Quasi-2D carrier transport in KMgBi for promising thermoelectric performance, ACS Appl. Energy Mater. **5**, 9141 (2022).
[23] X. Zhang, S. Sun, and H. Lei, Narrow-gap semiconducting properties of KMgBi with multiband feature, Phys. Rev. B **95**, 035209 (2017).
[24] P. Bordbar, B. Nedaee-Shakarab, and S. M. Khouzani, Thermodynamic phase diagram stability, electronic and thermoelectric properties of the half-Heusler KMgP [111] films, Indian J. Phys. **96**, 103 (2022).
[25] Q. Liu, Y. Liu, J. Xing, X. Jiang, and J. Zhao, A valence balancing rule for the design of bimetallic phosphides targeting high thermoelectric performance, Phys. Chem. Chem. Phys. **23**, 18916 (2021).
[26] J. W. Bennett, K. F. Garrity, K. M. Rabe, and D. Vanderbilt, Hexagonal *ABC* Semiconductors as Ferroelectrics, Phys. Rev. Lett. **109**, 167602 (2012).
[27] J. W. Bennett, K. F. Garrity, K. M. Rabe, and D. Vanderbilt, Orthorhombic *ABC* Semiconductors as Antiferroelectrics, Phys. Rev. Lett. **110**, 017603 (2013).
[28] M. Arif, G. Murtaza, R. Ali, R. Khenata, Y. Takagiwa, M. Muzammil, and S. B. Omran, Elastic and electro-optical properties of XYZ (X = Li, Na and K; Y = Mg; Z = N, P, As, Sb and Bi) compounds, Indian J. Phys. **90**, 639 (2016).
[29] Y. Xiao and L. D. Zhao, Charge and phonon transport in PbTe-based thermoelectric materials, npj Quantum Mater. **3**, 55 (2018).
[30] Y. Fu, Q. Zhang, Z. Hu, M. Jiang, A. Huang, X. Ai, S. Wan, H. Reith, L. Wang, K. Nielsch, and W. Jiang, $Mg_3(Bi,Sb)_2$-based thermoelectric modules for efficient and reliable waste-heat utilization up to 750 K, Energy Environ. Sci. **15**, 3265 (2022).
[31] G. Kresse and J. Hafner, *Ab initio* molecular dynamics for liquid metals, Phys. Rev. B **47**, 558(R) (1993).
[32] G. Kresse and J. Hafner, *Ab initio* molecular-dynamics simulation of the liquid-metal–amorphous-semiconductor transition in germanium, Phys. Rev. B **49**, 14251 (1994).
[33] G. Kresse and J. Furthmüller, Efficiency of ab-initio total energy calculations for metals and semiconductors using a plane-wave basis set, Comput. Mater. Sci. **6**, 15 (1996).
[34] G. Kresse and J. Furthmüller, Efficient iterative schemes for *ab initio* total-energy calculations using a plane-wave basis set, Phys. Rev. B **54**, 11169 (1996).
[35] G. Kresse and D. Joubert, From ultrasoft pseudopotentials to the projector augmented-wave method, Phys. Rev. B **59**, 1758 (1999).
[36] P. E. Blöchl, Projector augmented-wave method, Phys. Rev. B **50**, 17953 (1994).
[37] J. P. Perdew, K. Burke, and M. Ernzerhof, Generalized Gradient Approximation Made Simple, Phys. Rev. Lett. **77**, 3865 (1996).
[38] J. P. Perdew, A. Ruzsinszky, G. I. Csonka, O. A. Vydrov, G. E. Scuseria, L. A. Constantin, X. Zhou, and K. Burke, Restoring the Density-Gradient Expansion for Exchange in Solids and Surfaces, Phys. Rev. Lett. **100**, 136406 (2008).
[39] A. V. Krukau, O. A. Vydrov, A. F. Izmaylov, and G. E. Scuseria, Influence of the exchange screening parameter on the performance of screened hybrid functionals, J. Chem. Phys. **125**, 224106 (2006).
[40] J. Klimeš, D. R. Bowler, and A. Michaelides, Van der Waals density functionals applied to solids, Phys. Rev. B **83**, 195131 (2011).
[41] A. Togo and I. Tanaka, First principles phonon calculations in materials science, Scr. Mater. **108**, 1 (2015).
[42] A. Togo, L. Chaput, and I. Tanaka, Distributions of phonon lifetimes in Brillouin zones, Phys. Rev. B **91**, 094306 (2015).
[43] W. Li, J. Carrete, N. A. Katcho, and N. Mingo, ShengBTE: a solver of the Boltzmann transport equation for phonons, Comput. Phys. Commun. **185**, 1747 (2014).
[44] W. Li, L. Lindsay, D. A. Broido, D. A. Stewart, and N. Mingo, Thermal conductivity of bulk and nanowire $Mg_2Si_xSn_{1-x}$ alloys from first principles, Phys. Rev. B **86**, 174307 (2012).
[45] T. Feng and X. Ruan, Quantum mechanical prediction of four-phonon scattering rates and reduced thermal conductivity of solids, Phys. Rev. B **93**, 045202 (2016).
[46] T. Feng, L. Lindsay, and X. Ruan, Four-phonon scattering significantly reduces intrinsic thermal conductivity of solids, Phys. Rev. B **96**, 161201(R) (2017).
[47] Z. Han, X. Yang, W. Li, T. Feng, and X. Ruan, FourPhonon: An extension module to ShengBTE for computing four-phonon scattering rates and thermal conductivity, Comput. Phys. Commun. **270**, 108179 (2022).
[48] A. M. Ganose, J. Park, A. Faghaninia, R. Woods-Robinson, K. A. Persson, and A. Jain, Efficient calculation of carrier scattering rates from first principles, Nat. Commun. **12**, 2222 (2021).
[49] G. K. Madsen, J. Carrete, and M. J. Verstraete, BoltzTraP2, a program for interpolating band structures and calculating semi-classical transport coefficients, Comput. Phys. Commun. **231**, 140 (2018).
[50] L. Onsager, Reciprocal relations in irreversible processes. I., Phys. Rev. **37**, 405 (1931).
[51] See Supplemental Material at http://link.aps.org/supplemental/10.1103/PhysRevMaterials.7.095401 for pressure dependent lattice constants of KMgSb and KMgBi; pressure dependent power factor of KMgSb; pressure dependent phonon band structure, density of states, and Grüneisen parameter of KMgSb; pressure dependent electronic and thermal transport properties of KMgSb; electronic and thermal transport properties of Bi doped and As doped KMgSb; band structure of As doped KMgSb.
[52] G. A. Slack, The thermal conductivity of nonmetallic crystals, in *Solid State Physics*, edited by H. Ehrenreich, F. Seitz, and D. Turnbull, Solid State Physics Series Vol. 34 (Academic, New York, 1979), pp. 1–71, and references therein.
[53] A. She, Y. Zhao, J. Ni, S. Meng, and Z. Dai, Investigation on transport properties and anomalously heat-carrying optical phonons in KXY (X = Ca, Mg; Y = Sb, Bi), Int. J. Heat Mass Transfer **209**, 124132 (2023).
[54] T. Tadano, Y. Gohda, and S. Tsuneyuki, Anharmonic force constants extracted from first-principles molecular dynamics: applications to heat transfer simulations, J. Phys.: Condens. Matter **26**, 225402 (2014).
[55] T. Tadano and S. Tsuneyuki, Self-consistent phonon calculations of lattice dynamical properties in cubic $SrTiO_3$ with first-principles anharmonic force constants, Phys. Rev. B **92**, 054301 (2015).
[56] D. J. Singh and I. I. Mazin, Calculated thermoelectric properties of La-filled skutterudites, Phys. Rev. B **56**, R1650 (1997).